Liquid Crystals
Publication details, including instructions for authors and subscription information:
http://www.informaworld.com/smpp/title~content=t713926090

Phase diagram of new lactic acid derivatives exhibiting ferro- and antiferroelectric phases

Miroslav Kašpar[a]; Vladimíra Novotná[a]; Věra Hamplová[a]; Damian Pociecha[b]; Milada Glogarová[a]
[a] Institute of Physics, Academy of Sciences of the Czech Republic, 182 21 Prague 8, Czech Republic [b] Laboratory of Dielectrics and Magnetics, Chemistry Department, Warsaw University, 02-089 Warsaw, Poland

To cite this Article Kašpar, Miroslav , Novotná, Vladimíra , Hamplová, Věra , Pociecha, Damian and Glogarová, Milada(2008) 'Phase diagram of new lactic acid derivatives exhibiting ferro- and antiferroelectric phases', Liquid Crystals, 35: 8, 975 — 985
To link to this Article: DOI: 10.1080/02678290802308043
URL: http://dx.doi.org/10.1080/02678290802308043

Liquid Crystals,
Vol. 35, No. 8, August 2008, 975–985

Taylor & Francis
Taylor & Francis Group

Phase diagram of new lactic acid derivatives exhibiting ferro- and antiferroelectric phases

Miroslav Kašpar[a], Vladimíra Novotná[a]*, Věra Hamplová[a], Damian Pociecha[b] and Milada Glogarová[a]

[a]*Institute of Physics, Academy of Sciences of the Czech Republic, Na Slovance 2, 182 21 Prague 8, Czech Republic;* [b]*Laboratory of Dielectrics and Magnetics, Chemistry Department, Warsaw University, Al. Zwirki i Wigury 101, 02-089 Warsaw, Poland*

(Received 28 March 2008; final form 27 June 2008)

Rich polymorphism has been found in a new series of lactic acid derivatives. The length of a non-chiral *n*-alkyl chain plays an important role in changing the sequence and temperature range of phases. Except for one homologue with the shortest chain, all compounds exhibit a rather wide antiferroelectric chiral smectic C (SmC^*_A) phase below the ferroelectric (SmC*) and paraelectric smectic A (SmA) phases. The spontaneous polarisation and tilt angle were measured in the SmC* and SmC^*_A phases. For several compounds, small-angle X-ray diffraction measurements provided information about layer spacing, *d*. Temperature dependences, *d*(*T*), exhibit a rather large jump at the SmC*–SmC^*_A phase transition, but no anomaly was observed in the temperature dependences of the tilt angle and spontaneous polarisation. For one compound studied, a TGBA phase was established on the basis of the planar sample and free-standing film observation under a polarising optical microscope. For two compounds with the longest non-chiral chain, a direct phase transition from isotropic to the SmC^*_A phase was observed. All materials studied by dielectric spectroscopy revealed soft and Goldstone modes in the respective SmA and SmC* phases and two high-frequency modes in the SmC^*_A phase.

Keywords: ferroelectric liquid crystals; antiferroelectric phase; dielectric properties; lactate group; TGBA phase

1. Introduction

Since its discovery in 1979 in a liquid crystalline compound abbreviated as MHPOBC (*1*), the antiferroelectric chiral smectic C (SmC^*_A) phase has been observed in many substances. Nevertheless, whereas thousands of compounds form the ferroelectric smectic phase (SmC*), only hundreds examples of the SmC^*_A phase have been observed to date. Antiferroelectric liquid crystals are still of great interest due to their potential applications and scientifically interesting anticlinic structure. Great effort has been spent on obtaining a more complete understanding of the relationship between molecular structure and mesomorphic behaviour. Most compounds exhibiting the SmC^*_A phase have typically a molecular core composed of three aromatic rings, mostly based on biphenyl–phenyl linked by an ester group. When designing new liquid crystal molecules, one should remember that their mesogenic behaviour is influenced not only by the structure of the core but also by the chiral part of the molecule. Application of a single lactate unit as a basis of the chiral part has yielded many materials with a rather broad ferroelectric phase (*2–11*). Materials with two lactate units have been described in several papers (*12–15*) and among them some compounds exhibiting the antiferroelectric phase were reported. Recently, a series of ferroelectric liquid crystalline materials with two chiral centres, one of them being composed from the lactate unit, have been synthesised (*16*). These compounds show extremely broad temperature interval of the twisted grain-boundary (TGB) phase, which occurs probably due to a strong chiral force of this type of chain in combination with the type of the molecular core with biphenyl near the chiral part.

In this work, we attempted to combine a molecular core containing biphenyl and phenyl units connected by an ester [similar to the core used previously (*16*)] and prolonged by a promising chiral chain with two lactate units. In contrast with the MHPOBC prototype of antiferroelectric liquid crystals, we have applied the reverse sequence phenyl–biphenyl to modify the core. Such a type of a core used by Goodby *et al.* (*17*) yielded the TGB as well as the antiferroelectric phases. The chiral chain with three chiral centres (two lactate units and chiral methylbutyl) was expected to promote molecular chirality and flexibility and also affect liquid crystalline properties. The aim was to prepare compounds with an antiferroelectric phase over a broad temperature range approaching room temperature and to study the effect of the non-chiral chain length on mesomorphic properties.

*Corresponding author. Email: novotna@fzu.cz

ISSN 0267-8292 print/ISSN 1366-5855 online

DOI: 10.1080/02678290802308043
http://www.informaworld.com

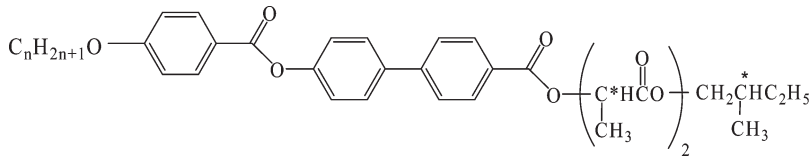

Scheme 1. Chemical formula of studied compounds designated as **HLL*n***, where *n* is the number of carbon atom in the alkyl chain.

2. Synthesis

The general formula of the studied compounds is shown in Scheme 1. The synthesis of the studied compounds, designated as **HLL*n***, was carried out according to the synthetic route described in Scheme 2. All chiral centres have the (*S*) configuration. The structures of all intermediates and final products were confirmed by ^{1}H NMR (300 MHz, $CDCl_3$, Varian, Gemini 2000) spectroscopy.

Preparation of alcohol 1

The synthesis of chiral alcohol **1** is described in detail by Wu and Lin (*8*). As starting materials we used commercial (*S*)-(−)-2-methylbutanol (Fluka, 99.5%, $[\alpha]^{20}_D = -6.3$; c=10 in ethanol) and L-(+)-lactic acid (Fluka). L-(+)-lactic acid (ca. 80% solution in water) was prepared by fermentation and contained less than 1% of D-isomer. After esterification, we obtained alcohol **1** with optical rotation $[\alpha]^{20}_D = -47.5^\circ$ (neat), b.p. 108–111°C/2 torr.

Preparation of phenol 2

Chiral alcohol **1** was esterified by protected 4-hydroxy-4′-biphenylcarbonyl chloride in pyridine/dichloromethane mixture followed by ammonolysis in a chloroform/tetrahydrofuran mixture at 10°C. After separation of the reaction mixture by column chromatography on silica gel (using a mixture of dichloromethane and acetone 99:1 as the eluent) phenol **2** was obtained in 50% yield. ^{1}H NMR ($CDCl_3$, 300 MHz): 8.1 (d, 2H, ortho to –COO), 7.58 (d, 2H, meta to –COO), 7.42 (d, 2H, meta to –OH), 6.90 d, 2H, ortho to –OH), 5.4 (q, 1H, ArCOOCH*), 5.22 (q, 1H, C*HCOOCH$_2$), 4.0 (m, 2H, COOCH$_2$), 1.75 (d, 3H,

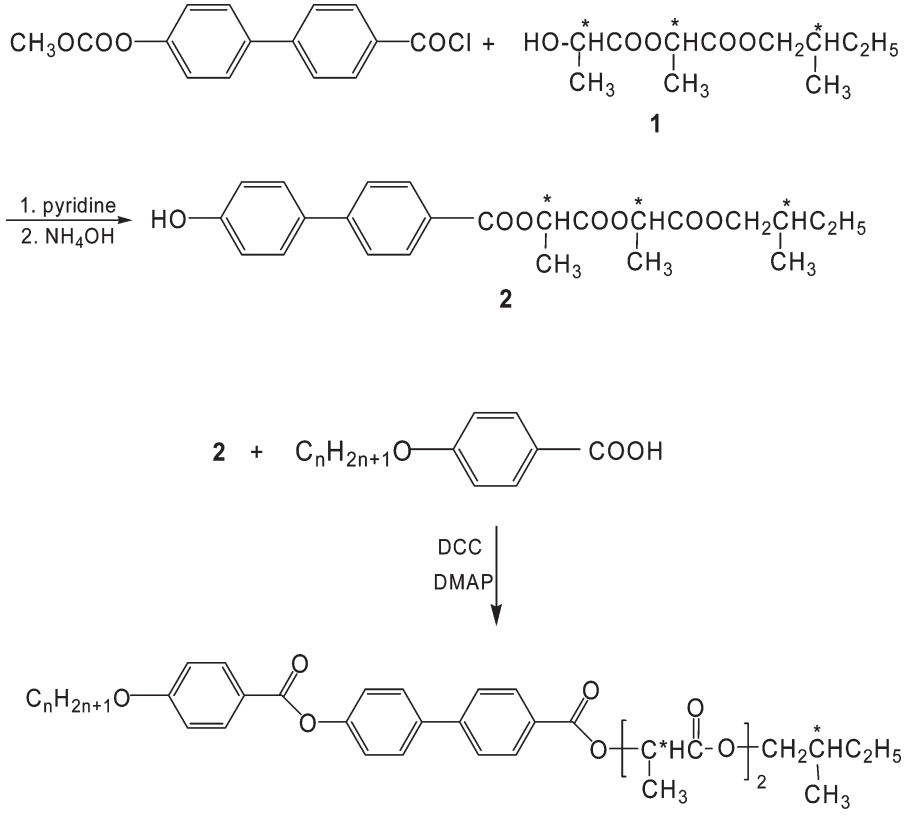

Scheme 2. Schematic route for synthesis of **HLL*n***.

$\underline{CH_3}CHCOO$), 1.58 (d, 3H, $\underline{CH_3}CHCOOCH_2$), 1.2–1.7 (m, 3H, CH–$CH_2$), 0.9 (m, 6H, CH_3).

Preparation of final products

The final products (**HLL*n***) were prepared by standard methods of esterification with dicyclohexylcarbodiimide (DCC) in the presence of dimethylaminopyridine (DMAP) in dichloromethane. Crude products were purified by column chromatography on silica gel using a mixture of dichloromethane and acetone (99.5:0.5) as eluent and crystallised twice from mixture of ethanol and acetone. Structures of all final products were confirmed by ^{1}H NMR measurements. The chemical purity of compounds was checked by high-pressure liquid chromatography (HPLC), which was carried out with an Watrex HPLC chromatograph using a silica gel column (Biospher Si 5 µm, 4 × 250, Watrex) with a mixture of 99.9% of toluene and 0.1% of methanol as eluent, and detection of the eluting products by a UV-visible detector (λ=290 nm). The chemical purity was found better than 99.8% under these conditions.

For example, for **HLL7**, ^{1}HNMR ($CDCl_3$, 300 MHz): 8.18 (d, 4H, ortho to –COO), 7.68 (d, 4H, ortho to –Ar), 7.30 (d, 2H ortho to –OCO), 7.00 (d, 2H, ortho to –OR), 5.40 (q, 1H, CH*), 5.25 (q, 1H, $\underline{C^*H}COOCH_2$), 4.05 (m, 4H, CH_2OAr and $COOCH_2$), 1.75 (d, 3H, CH_3C^*), 1.60 (d, 3H, $\underline{CH_3}CHCOOCH_2$), 1.2–1.9 (m, 13H, CH+$CH_2$), 0.9 (m, 9H, CH_3).

3. Experimental

The liquid crystalline phases were identified firstly by texture observation using a polarising optical microscope (Nikon Eclipse E-600). Most studies were carried out on samples in planar geometry with a sample thickness of 6, 25 or 50 µm. The cells, which were composed of glass plates provided with ITO electrodes and unidirectionally rubbed polyimide layers, were filled in the isotropic phase. Temperature was changed and stabilised with accuracy of $\pm$0.1 K in the hot stage (Linkam) placed on the working place of the polarising optical microscope. In addition, free-standing films were observed, in which the liquid crystalline material was spread over a circular hole (diameter 3 mm) in a metallic plate.

Phase transition temperatures and corresponding enthalpies were determined by differential scanning calorimetry (DSC, Perkin–Elmer Pyris Diamond). Samples of about 3 mg were hermetically sealed in aluminium pans. Heating and cooling rates of 5 K min^{-1} were applied subsequently.

The spontaneous polarisation, P_s, was determined from $P(E)$ hysteresis loops taken at a frequency of 50 Hz. The spontaneous tilt angle, θ_s, was determined from the angle difference between minimum transmission (extinction) positions with crossed polarisers under the opposite dc electric fields.

X-ray diffraction measurements were performed with Bruker D8 Discovery diffractometer equipped with Paar DCS350 heating stage allowing temperature control with a precision of 0.1 K. Experiments were performed in the reflection mode from one surface free sample. The length of molecules was calculated using Chem3D software (CambridgeSoft Corporation).

Dielectric properties were studied using a Schlumberger 1260 impedance analyser. The frequency dispersions were measured on cooling at a rate of about 0.2 K min^{-1}, keeping the temperature of the sample stable during frequency sweeps in the range 10 Hz–1 MHz. In the SmA, TGBA and SmC* phases the frequency dispersion data were analysed using the modified Cole–Cole formula for the frequency dependent complex permittivity $\varepsilon^*(f)=\varepsilon' - i\varepsilon''$:

$$\varepsilon^* - \varepsilon_\infty = \frac{\Delta\varepsilon}{1+(if/f_r)^{(1-\alpha)}} - i\left(\frac{\sigma}{2\pi\varepsilon_0 f^n} + Af^m\right), \quad (1)$$

where f_r is the relaxation frequency, $\Delta\varepsilon$ is dielectric strength, α is the distribution parameter of the relaxation, ε_0 is the permittivity of a vacuum, ε_∞ is the high frequency permittivity and *n, m, A* are parameters. The second and third terms in the formula are used to eliminate a low-frequency contribution from dc conductivity and a high-frequency contribution due to resistance of the electrodes, respectively. Real and imaginary parts of the permittivity were fitted simultaneously using the Scientist program (MicroMaths Scientist Software Corporation). Especially for dielectric spectroscopy in the SmC*$_A$ phase, where high-frequency modes occur, we prepared cells from glass plates equipped by evaporated non-transparent gold electrodes. The higher conductivity of the gold electrodes compared to that of ITO ones shifted the cut-off frequency up to 10 MHz. The modified Cole–Cole formula for description of two modes in the SmC*$_A$ phase was used in the following form, the low frequency contribution being ignored:

$$\varepsilon * - \varepsilon_\infty = \frac{\Delta\varepsilon_1}{1+(if/f_1)^{(1-\alpha 1)}} + \frac{\Delta\varepsilon_2}{1+(if/f_2)^{(1-\alpha 2)}} - iAf^m. \quad (2)$$

Table 1. Melting point (m.p.) indicated on second heating and phase transition temperatures, T_c, and corresponding enthalpies, ΔH, detected on second cooling (in square brackets) are in kJ/mol. All thermograms were recorded at a rate of $5\,K\,min^{-1}$. Designation of compounds corresponds to that shown in Scheme 1.

	m.p./°C [ΔH]	T_{cr}/°C [ΔH]	SmC_A*	T_c/°C [ΔH]	SmC*	T_c/°C [ΔH]	SmA	T_c/°C [ΔH]	TGBA	T_c/°C [ΔH]	I
HLL6	51 [+25.7]	37 [−4.0]	—		•	51 [−0.02]	•	108 [−3.5]	—		•
HLL7	55 [+26.7]	28 [−0.7]	•	52 [−0.06]	•	67 [−0.05]	•	102 [−3.1]	—		•
HLL8	50 [+16.5]	27 [−2.1]	•	60 [−0.03]	•	71 [−0.03]	•	100 [−3.0]	—		•
HLL9	32 [+3.0]	31 [−3.0]	•	72 [−0.10]	•	79 [−0.07]	•	92 [−1.6]	—		•
HLL10	32 [+2.95]	36 [−3.7]	•	75 [−0.83]	•	80 [−0.14]	—		•	86 [−1.0]	•
HLL11	37 [+5.25]	36 [−5.1]	•	76 [−1.05]	—		—		—		•
HLL12	40 [+23.5]	38 [−4.5]	•	78 [−1.10]	—		—		—		•

4. Results

Mesomorphic properties

The phase transition temperatures and the enthalpies were evaluated from DSC studies. Phases were determined from observations of textures and their changes and from another experimental technique described below. Results are summarised in Table 1. The phase diagram for all compounds is shown in Figure 1; *n* is the number of carbon atoms in the alkyl chain. **HLL6** with the shortest non-chiral chain ($n=6$) exhibits a SmA–SmC* phase sequence on cooling, the SmC* phase being monotropic. For all other studied compounds, the antiferroelectric phase occurs. **HLL7**, **HLL8** and **HLL9** exhibit a SmA–SmC*–SmC^*_A phase sequence. The SmC*–SmC^*_A phase transition is monotropic for **HLL7**. For **HLL10** the TGBA–SmC*–SmC^*_A phase sequence was found. Typical features of textures in planar samples and in free standing films are described below. The entalphy value connected with the SmC*–SmC^*_A phase transition is small for **HLL7** and **HLL8**, typical for such a type of phase transition (*18*). For **HLL9** and **HLL10** it is a bit higher, but it is still more than one order smaller than the typical transition enthalpy to the hexatic phases (*12, 18, 19*). Moreover, the profile of the DSC peak connected with the transition to the hexatic phases is quite characteristic having symmetrical broad wings on both sides (*19*), which is not found for the compound reported here. From these reasons we could exclude the possibility of the SmC*–hexatic phase transition for the studied compound (will be supported by texture observation below). The antiferroelectric character of the SmC^*_A phase was confirmed by dielectric and switching studies. For compounds with the longest alkyl chain (**HLL11** and **HLL12**) the SmC^*_A phase is reached directly from the isotropic phase on cooling.

Typical thermographs taken on cooling are shown in Figure 2 for **HLL8**, **HLL9** and **HLL10**. For

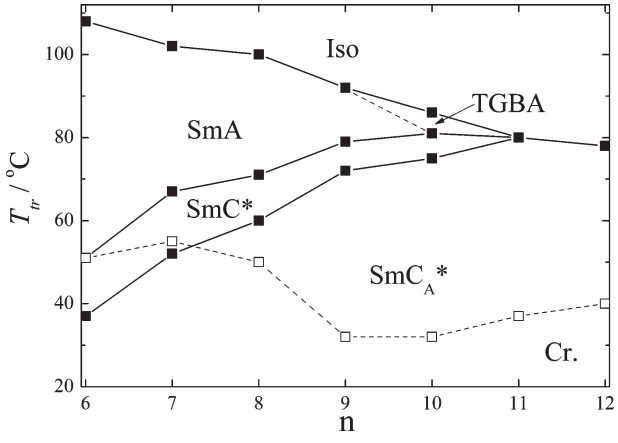

Figure 1. Graphical presentation of the mesomorphic properties of the studied compounds (*n* represents the number of carbons in the non-chiral chain). Phases are designated, empty symbols are melting points.

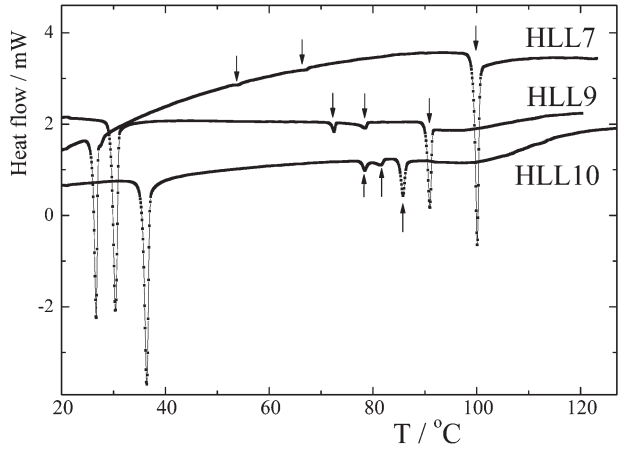

Figure 2. DSC thermograms for designated compounds taken on second cooling at a rate of $5\,K\,min^{-1}$. Arrows indicate the isotropic–SmA (TGBA phase for **HLL10**), SmA–SmC* and SmC*–SmC^*_A phase transitions subsequently on cooling.

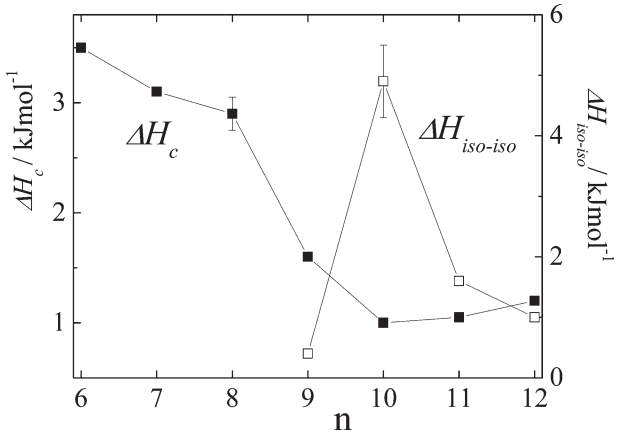

Figure 3. Enthalpies of the isotropic–SmA (TGBA or SmC*$_A$), ΔH_c (full symbols), and the isotropic–isotropic, $\Delta H_{iso\text{-}iso}$ (open symbols), phase transitions versus *n*-alkyl chain length.

HLL10, which exhibits the TGBA phase, a marked broad diffuse peak is seen in the temperature range of isotropic phase in both cooling and heating cycles. A similar but not so marked peak is also seen in the next homologue **HLL9**, where no TGB phase occurs (see Figure 2). In this temperature range, no effects were observed under the polarising microscope or using the other experimental technique.

We have examined the variation of the enthalpy detected on cooling from the isotropic phase, ΔH_c, with respect to the chain length for all compounds studied. The dependence of ΔH_c on the number of alkyl units in the non-chiral chain is shown in Figure 3. A sharp decrease of ΔH_c on ascending the chain length is evident when approaching the TGBA phase (n=10). In addition, the enthalpy connected with the broad diffuse peak in the isotropic phase, $\Delta H_{iso\text{-}iso}$, is included in Figure 3. There is a pronounced maximum for **HLL10**, but the $\Delta H_{iso\text{-}iso}$ value remains non-zero even for the nearby homologues (n=9, 11 and 12).

Texture observation

The phases were identified according to texture observations under a polarising optical microscope. Planar samples for compounds with n=6–9 exhibited a typical fan-shaped texture in the SmA phase, which transforms into the broken fan-shaped texture in the SmC* phase on cooling. The SmC*–SmC*$_A$ phase transition has first-order character and proceeds as a step-like change of the birefringence in planar texture for all compounds, the phase coexistence being observed. No other changes in the texture are observed during this phase transition, which confirms the SmC*$_A$ structure in the low temperature phase. In free-standing films, the typical schlieren texture was observed in both tilted SmC* and SmC*$_A$ phases.

For **HLL10**, various planar textures were observed on cooling from the isotropic phase (see Figure 4). The blurred coloured fans typical for the TGBA phase were often observed in thicker samples, 10 µm or higher (Figure 4(a)). In thinner samples (typically less than 5 µm), the texture exhibits features of the cholesteric phase (Figure 4(b)) or the texture shown in Figure 4(c). It may happen that the former is reconstructed to the latter on cooling. A bias electric field of about 1 V µm^{-1} transforms the TGBA to the SmA phase. After the field is switched off, the TGBA texture is slowly restored in the form of the blurred coloured fans. In the free-standing films, a

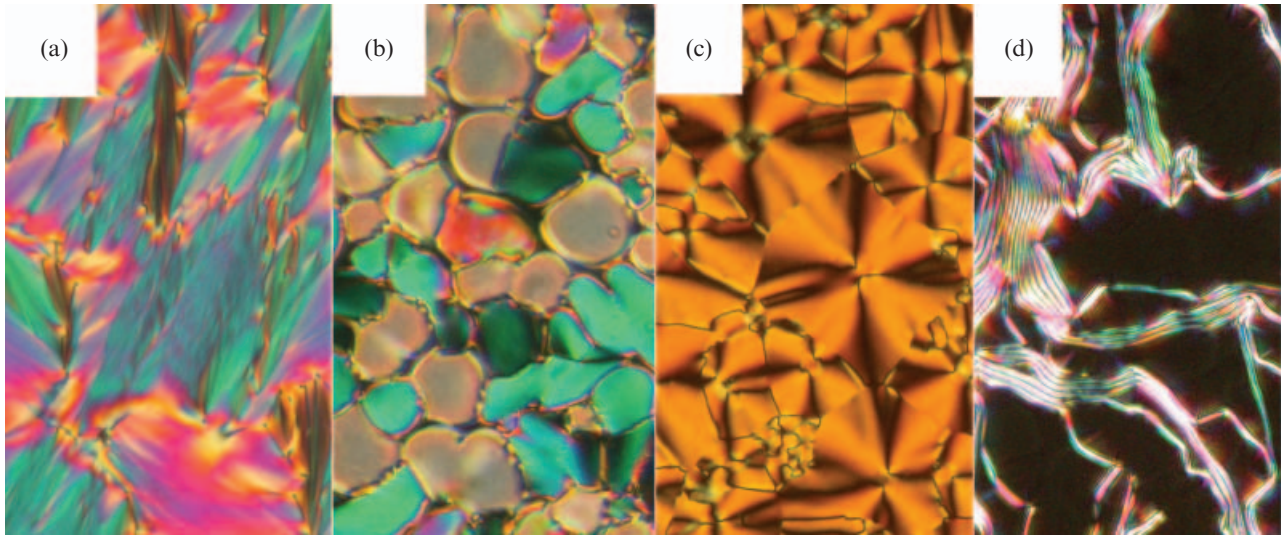

Figure 4. Photomicrographs taken in the TGBA phase of **HLL10**. Planar textures for (a) cell of 12 µm, (b, c) 5 µm (Linkam cell) and (d) sample with one free surface. The width of the photomicrographs is about 150 µm.

filament texture (Figure 4(d)) was observed, which is typical for the TGBA phase (*20*). The phase transition from the TGBA to the SmC* phase is connected with a complete reconstruction of the texture across a phase boundary, which is significant for the first-order transition.

For homologues with $n=11$ and 12, the SmC*$_A$ phase appears on cooling just below the isotropic phase.

Spontaneous quantities and switching properties

Temperature dependences of the spontaneous polarisation, $P_s(T)$, and spontaneous tilt angle, $\theta_s(T)$, were measured on cooling from the SmA to the SmC* and SmC*$_A$ phases (see Figure 5). Within the SmC*$_A$ phase the coercive field increases on cooling so that the measurement cannot be accomplished down to the crystallisation. For both quantities, a discontinuity at the SmA–SmC* phase transition increases with increasing length of non-chiral chain (n value) starting from a nearly continuous second-order phase transition detected for the shortest homologue **HLL6**.

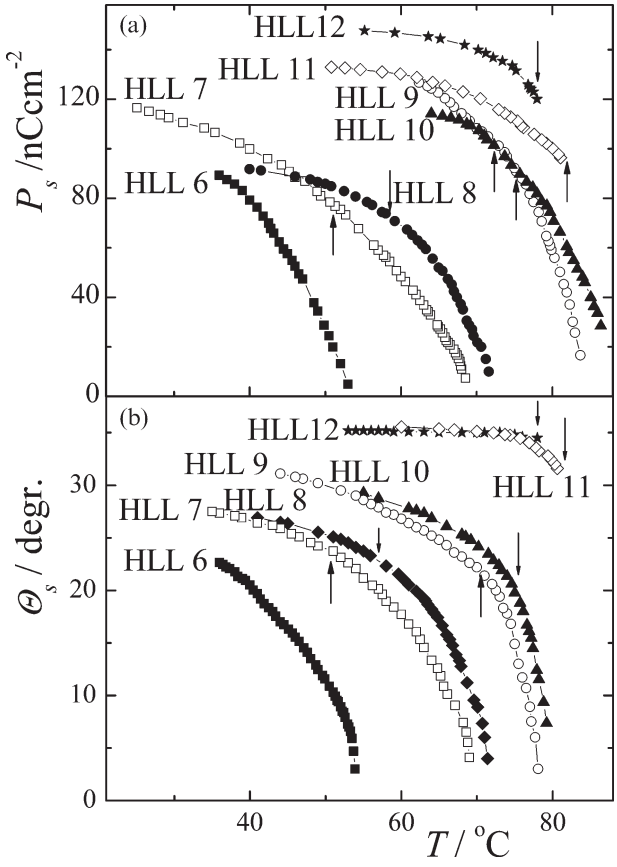

Figure 5. Temperature dependences of (a) spontaneous polarisation and (b) tilt angle measured on cooling. Compounds are designated. Arrows indicate the phase transition to the SmC*$_A$ phase.

The TGBA–SmC* phase transition for **HLL10**, as well as the transition from the isotropic to the SmC*$_A$ phase for **HLL11** and **HLL12**, proceed in a discontinuous way, showing clearly that they are first-order phase transitions. The highest P_s and θ_s values are found for **HLL11** and **HLL12**, reaching about 140 nC cm^{-2} and 35°, respectively, in saturated values. In other compounds, the P_s and θ_s values increase with n and exhibit no saturation on cooling. For all studied compounds, no anomaly was detected at the SmC*–SmC*$_A$ phase transition, either in $P_s(T)$ or in $\theta_s(T)$ dependences (see Figure 5). This is not surprising since both spontaneous values were measured under electric fields strong enough to transform the anticlinic into the synclinic structure and thus the information about the SmC*–SmC*$_A$ structural changes is lost.

X-ray measurements

Temperature dependences of the layer spacing, $d(T)$, are shown in Figure 6 for **HLL8, HLL9** and **HLL10**. In the SmA phase, a slight increase of $d(T)$ values is seen on cooling, which is usually explained by an increase of the nematic order parameter (*21*). The same is observed in the TGBA phase. At the onset of the SmC* phase on cooling, $d(T)$ shows a significant decrease, which reflects the tilt of the molecules. At the SmC*–SmC*$_A$ phase transition, $d(T)$ exhibits another jump decrease. On further cooling within the SmC*$_A$ phase, d starts to increase gradually due to the stretching of aliphatic molecular chains (*22*). In Figure 7, the temperature dependence, $d(T)$, is presented together with the scattered X-ray intensity, a quantity that is related to the degree of molecular order. The oscillation of intensity values at the

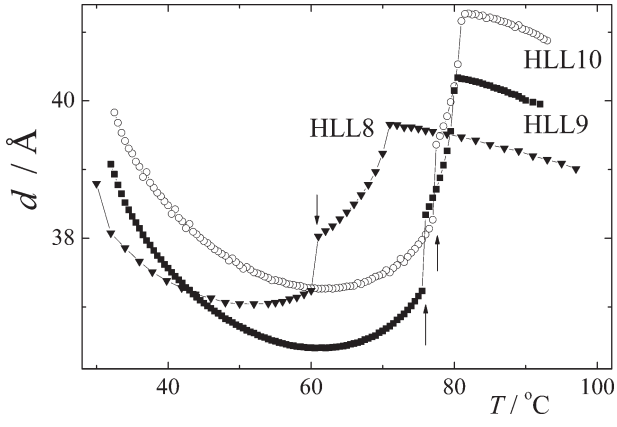

Figure 6. Results of X-ray measurements showing the temperature dependences of the layer spacing for **HLL8**, **HLL9** and **HLL10** taken on cooling from the isotropic phase. Compounds are designated; arrows mark the SmC*–SmC*$_A$ phase transition.

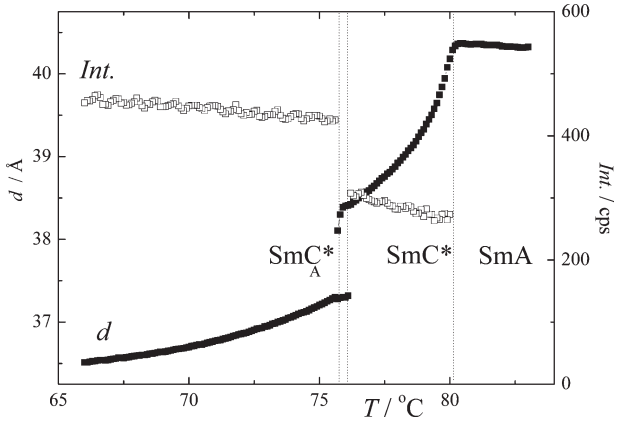

Figure 7. Temperature dependences of the layer spacing, d (full symbols), and X-ray signal intensity (open symbols) for **HLL9**. Phases are designated, arrows mark the corresponding axis.

SmC*–SmC*$_A$ phase transition is probably connected with the coexistence of both phases.

We have compared the spontaneous tilt angle measured optically (see above) and the value of molecular inclination calculated from the layer spacing measurement. For calculation, the layer spacing at the SmA–SmC* transition was taken as a reference. For **HLL10**, the results are shown in Figure 8. The accuracy of such a comparison depends on exactly establishing the phase transition temperature as well as calibration of X-ray apparatus.

Dielectric spectroscopy

The dielectric spectroscopy data show just one distinct mode in the SmA, TGBA and SmC* phases. Fitting the data using equation (1) yields values of the

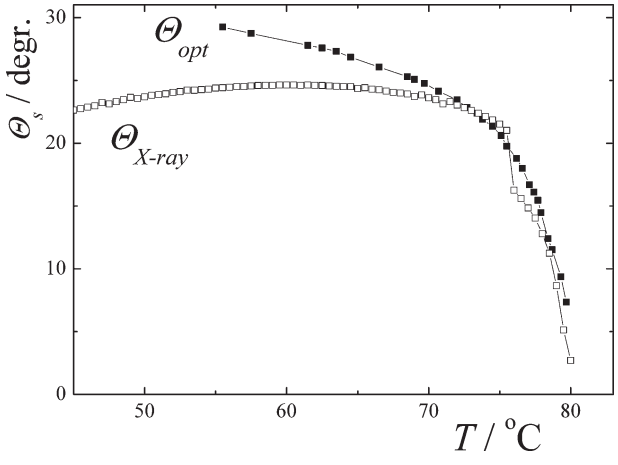

Figure 8. Comparison of tilt angle measured optically, Θ_{opt} (full symbols), and tilt of molecules calculated from the layer spacing measurement, $\Theta_{X\text{-}ray}$ (open symbols), for **HLL10**.

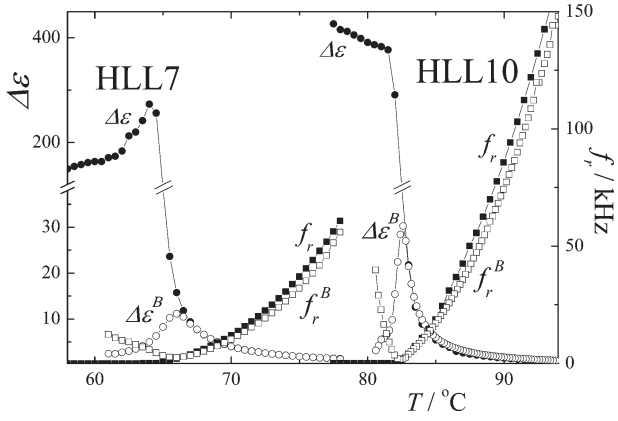

Figure 9. Temperature dependences of the dielectric strength, $\Delta\varepsilon$ (circles), and the relaxation frequency, f_r (squares), obtained by fitting the spectroscopic data for **HLL10** and **HLL7** in the TGBA–SmC* and SmA–SmC* temperature ranges. Full symbols are used for measurements without bias field; open symbols show measurement under applied bias of $1\,V\,\mu m^{-1}$ (upper symbol B).

relaxation frequencies, f_r, and dielectric strengths, $\Delta\varepsilon$, (see Figure 9). In the SmA phase, f_r of the mode decreases strongly on cooling and $\Delta\varepsilon$ is very low, with the exception of a slight increase, which occurs when approaching the phase transition to the SmC* phase. Such behaviour is typical for the soft mode (fluctuation of the molecular tilt). In the SmC* phase, the Goldstone mode (fluctuation of the azimuthal molecular orientation) takes place, which shows characteristic high $\Delta\varepsilon$ and low f_r values (Figure 9). No significant qualitative differences were found between the soft mode detected in the TGBA phase and the soft mode in other homologues exhibiting the SmA phase.

Under a bias field, the soft mode in the SmA phase is only weakly affected, which is expressed by a very slight decrease of f_r (Figure 9). In the SmC* phase, the Goldstone mode is eliminated, because the helical structure, which is the origin of this mode, is completely unwound by a sufficiently high bias field. Then the weak soft mode, which exists in the SmC* phase and is normally overwhelmed by the Goldstone mode, becomes visible within both SmA and SmC* phases. $\Delta\varepsilon$ values exhibit a maximum and f_r a minimum at the SmA–SmC* phase transition and the mode becomes non-visible near below this phase transition (Figure 9). Under the bias field, the TGBA phase is transformed to the SmA phase. It is rather surprising that for **HLL10** the soft mode of the TGBA phase is practically non-affected when this phase is transformed to the SmA phase by the bias field (see Figure 9).

In the antiferroelectric SmC*$_A$ phase, two modes occurs with very low $\Delta\varepsilon$ values and relative high

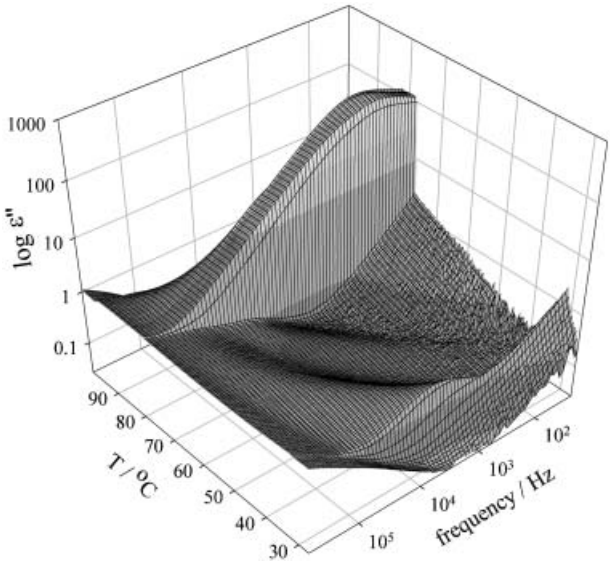

Figure 10. Three-dimensional plot of the imaginary part of dielectric permittivity for **HLL10**.

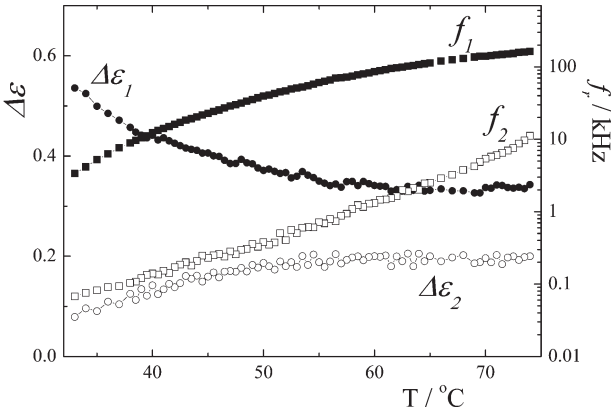

Figure 11. Temperature dependences of the dielectric strength, $\Delta\varepsilon$ (open symbols), and the relaxation frequency, f_r (full symbols), for two modes detected in the SmC*$_A$ phase of **HLL9**.

relaxation frequency for all compound exhibiting this phase ($n \geq 7$), although both modes are distinctly visible (see Figure 10). Results of fitting of the spectroscopic data in the antiferroelectric phase using equation (2) yield $\Delta\varepsilon$ and f_r values for both modes (see Figure 11 for **HLL9**). The relaxation frequencies of both modes decrease on cooling (Figure 11), dielectric strength $\Delta\varepsilon_1$ increases and $\Delta\varepsilon_2$ is nearly temperature independent and slightly decreases at low temperatures.

5. Discussion and conclusions

We have succeeded in preparation of compounds (**HLL*n***) with a very wide antiferroelectric phase temperature interval. For homologues with n=9–12, this phase is stabilised within about 40 K; for n=8 a part of its temperature range lies below the melting point. For n=7, the SmC*$_A$ phase is monotropic and for n=6 this phase does not exist. For n=7–10 homologues, the SmC*$_A$ phase is reached by cooling the SmC* phase; a direct phase transition from the isotropic to the antiferroelectric phase takes place for compounds with the longest non-chiral chain (n=11 and 12). The SmA phase exists above the SmC* phase in n=6–9 homologues, being narrower for increasing n. The narrowing of the SmA phase is connected with decreasing transition enthalpy from the isotropic phase, ΔH_c, (Figure 3). For the n=10 homologue, the SmA phase is replaced by a TGBA phase and ΔH_c is minimal, showing a rather weak first-order transition. In this case, strong pre-transitional phenomena are expected within the isotropic phase. In previous studies (*17, 23*), such phenomena manifested as a broad diffuse peak in the DSC plot have been found for several homologue series exhibiting the TGBA phase and assigned to the existence of an intermediate phase above the clearing temperature. The origin and structure of this phase has not yet been specified. The existence of the pre-transitional phenomena has been considered as a criterion for occurrence of the defect-stabilised TGBA phase (*17*). We have found a broad diffuse anomaly within the isotropic phase with the homologue exhibiting the TGBA phase, the enthalpy connected with this anomaly being rather high ($5\,\mathrm{kJ\,mol^{-1}}$). For the neighbouring homologue, **HLL9**, this anomaly is much lower but still persists, indicating that the free energy of the TGBA phase would not be much higher than the energy of the SmA phase exhibited by this compound.

The behaviour of the layer spacing, d, in the SmA phase, i.e. the observed increase of $d(T)$ on cooling (Figure 6), is quite typical and used to be explained by an increase of the effective molecular length (the projection of the molecule on the layer normal), which may occur due to the increase of molecular orientational order (nematic order parameter) (*21*). We have proved here that the same behaviour is present in the TGBA phase. Below the SmA–SmC* phase transition, d values decrease reflecting the increase of the molecular tilt. A strong anomaly has been found at the SmC*–SmC*$_A$ phase transition (Figure 6): the drop in $d(T)$ dependence is accompanied by a jump up in the intensity of X-ray signal (Figure 7). Two opposite tendencies can play a role in the SmC$_A$* phase that influence the d values. One is so-called dimerisation effect (*22, 24*), which causes the decrease of the layer spacing mainly at the SmC*–SmC*$_A$ phase transition; the other is stretching of aliphatic chains, which causes increase of $d(T)$ on cooling in the low temperature part of the SmC*$_A$

phase. The competition of both effects is responsible for the magnitude of the jump as well as for the non-monotonous temperature dependence of d within the SmC^*_A phase. It is necessary to point out that such a large jump in the layer spacing at the SmC^*–SmC^*_A phase transition as found in the compounds studied here has not been observed previously. We suppose that a non-continuous increase of the tilt angle could also contribute to this jump. Such an increase is not accessible by measurement under the bias field (see section on spontaneous quantities and switching properties), but still can occur because of the non-continuous phase transitions between the smectic tilted phases (*25*). This has also been confirmed for MHPOBC, by measurement of birefringence (*26*).

A comparison of the tilt angle measured optically on unwound structures with that calculated from the layer spacing temperature dependence is shown in Figure 8. For the temperature interval of the SmC^* phase the data obtained from both methods are not very different. It is slightly surprising because X-ray data are often found less than tilt from electro-optical measurements for conventional ferroelectrics. The jump of tilt at the SmC^*–SmC^*_A phase transition calculated from the jump of d amounts to 5°. In the SmC^*_A phase range there is a significant deviation of the tilt directly measured and calculated from X-ray, which is very frequently the case for an antiferroelectric phase. This deviation can be understood when stretching of aliphatic chain, which elongates the molecules, is taken into account. Then the calculation of molecular tilt based on a fixed molecular length cannot give proper results.

The scattered X-ray intensity can also give evidence on the degree of the molecular order (see Figure 7). The intensity slightly grows on cooling from the SmA–SmC^* phase transition and jumps up at the SmC^*–SmC^*_A phase transition, which gives evidence on the increase of smectic layer order (*22*).

Dielectric spectroscopy established the soft mode in the SmA as well as in the TGBA phases, the dielectric strength, $\Delta\varepsilon$, being higher and temperature dependence of the relaxation frequency, f_r, being more steep in the TGBA phase. The experimental data reported by Ismaili *et al.* (*27*) revealed a soft mode in the TGBA phase, with $\Delta\varepsilon$ much lower and f_r much higher compared with the SmA phase in the next homologue. They explained this difference on the basis of a modified Landau free energy, taking into account the elastic strain connected to the anchoring at the grain boundaries and the distance between them. We suppose that in our results the anchoring effects at the grain boundaries play no significant role as the soft mode remains practically unaffected by a strong bias field that transforms the TGBA phase to the SmA phase. The $\Delta\varepsilon$ of the soft mode (accessible in the SmC^* phase only under bias field) exhibits surprisingly high peak at the phase transition to the SmC^* phase for both compounds **HLL7** and **HLL10**. This fact evidences about strong tilt-angle (soft-mode) fluctuation and deserves other study.

The interpretation of modes in the SmC^*_A phase is not quite straightforward. The frequency relaxation in the range of hundred kHz or higher, depending on the temperature range, can be attributed to rotation of molecules about the short axis (non-collective mode) and thus its relaxation frequency should obey the Arrhenius law,

$$f_r = f_0 \exp(-E_a/RT), \tag{3}$$

which gives a linear dependence, $\ln f_r \approx 1/RT$, where T is the absolute temperature, R ($=8.314\,\mathrm{J\,mol^{-1}}$) is the universal constant, E_a is an activation energy and f_0 is a fitting parameter. The test of our experimental results with the Arrhenius formula is shown in Figure 12 for two compounds. For the others, the results are qualitatively the same and the one curve lies over the others. The linear dependence is fulfilled only for the low-frequency mode, which can hardly be a non-collective mode. Two collective modes used to be considered to contribute to permittivity in the SmC^*_A phase, namely the anti-phase and in-phase azimuthal motions of molecules in neighbouring layers; the latter could be dielectrically active due to the non-compensated polarisation in the helical structure (*28–32*). Recently, a theory has been worked out showing that the in-phase mode can be detected only under a bias electric field (*33, 34*). Then without the bias only one collective mode could occur.

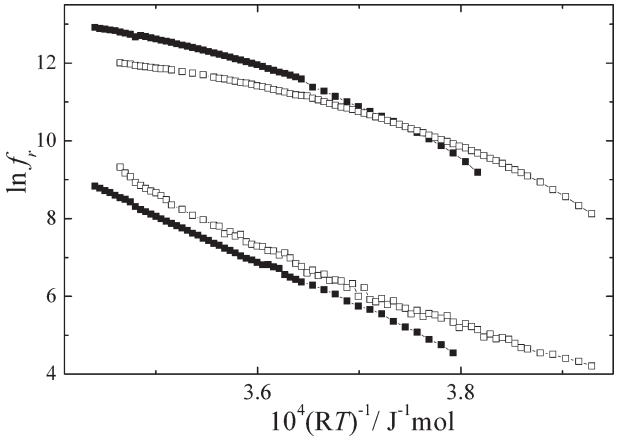

Figure 12. Arrhenius plot displays the logarithm of relaxation frequencies in the SmC^*_A phase versus reciprocal temperature for two compounds: **HLL9** (empty symbols) and **HLL12** (full symbols).

Taking into account this finding, we suggest that the detected mode with the lower f_r is the anti-phase collective mode and thus the one with the higher f_r has to correspond to the rotation of molecules around their short axes. The departure of the high f_r temperature dependence from the Arrhenius law can be caused by the low temperature deviation (on the right side of Figure 12) due to increase of the rotational viscosity.

Let us compare the properties of the presented **HLL*n*** series with previously studied compounds labelled ZLL (*12*). Molecules of both HLL and ZLL series have the same chiral and non-chiral chain, the only difference is in the core, namely in the reverse sequence of the phenyl and the biphenyl interconnected with the ester group. The presence of the chiral chain with two lactate units and 2-methylbutyl ensures anticlinic ordering and very similar values of the spontaneous polarisation and the tilt angle for both types of the core. A surprising effect has been found in the temperatures range of mesophases of compared compounds. The compounds of series **HLL*n*** have much lower transition temperatures, lowered by more than 25°C. We suppose that the position of the ester group in the core can influence the shape of the molecules, which can make their packing more difficult and thus lower the transition temperatures. On the other hand, the mere interchange of the same phenyl–biphenyl core sequence need not change the transition temperatures. Series with the same molecular core as reported here but with one lactate group in the chiral chain exhibit the same transition temperatures for both reversed cores (*35, 36*). Additionally, similar transition temperatures have been found for other series with reversed core and one chiral methylheptyl centre (*37*). It seems that the character of the chiral chain as well as its interaction with the core are essential for lowering the transition temperatures when reversing the phenyl–biphenyl sequence interconnected by an ester group in the case of the present compounds, **HLL*n***. The mechanism of such pronounced effect is still not clear and needs a more detailed analysis.

Acknowledgements

This work was supported by Research Project AVOZ 10100520, Projects No. IAA100100710 from Grant Agency of the Academy of Sciences of the Czech Republic, Czech-Polish bilateral collaboration program No.8 (2006-2007) under the Ministry of Education, Youth and Sports of the Czech Republic. The X-ray diffraction measurements were accomplished at the Structural Research Laboratory, Chemistry Department, University of Warsaw, Poland, which has been established with financial support from European Regional Development Found, project no: WKP 1/1.4.3./1/2004/72/72/165/2005/U.

References

(1) Chandani A.D.L.; Gorecka E.; Ouchi Y.; Takezoe H.; Fukuda A. *Jap. J. Appl. Phys.* **1989**, *28*, L1265–L1268.
(2) Tsai W.-L.; Lu T.-C.; Liu H.-W.; Tsai M.-Y.; Fu C.M. *Liq. Cryst.* **2000**, *27*, 1389–1392.
(3) Taniguchi H.; Ozaki M.; Yoshino K.; Satoh K.; Yamasaki N. *Ferroelectrics* **1988**, *77*, 137–144.
(4) Tsai W.-L.; Yeh S.-W.; Hsie M.-J.; Lee H.-C.; Fu C.-M. *Liq. Cryst.* **2002**, *29*, 251–253.
(5) Matsushima J.; Takanishi Y.; Ishikawa K.; Takezoe H.; Fukuda A.; Park C.S.; Jang W.-G.; Kim K.-H.; Maclennan J.-E.; Glaser M.A., et al. *Liq. Cryst.* **2002**, *29*, 27–37.
(6) Mery S.; Lottzsch D.; Heppke G.; Shashidhar R. *Liq. Cryst.* **1997**, *23*, 629–644.
(7) Wu S.L.; Lin C.Y. *Liq. Cryst.* **2002**, *29*, 1575–1580.
(8) Wu S.L.; Lin C.Y. *Liq. Cryst.* **2004**, *31*, 1613–1617.
(9) Wu S.L.; Lin C.Y. *Liq. Cryst.* **2005**, *32*, 1243–1249.
(10) Dzik E.; Mieczkowski J.; Gorecka E.; Pociecha D. *J. Mater. Chem.* **2005**, *15*, 1255–1262.
(11) Wu S.-L.; Hsu H.-N. *Liq. Cryst.* **2007**, *34*, 1159–1165.
(12) Kašpar M.; Hamplová V.; Novotná V.; Glogarová M.; Pociecha D.; Vaněk P. *Liq. Cryst.* **2001**, *28*, 1203–1209.
(13) Novotná V.; Kašpar M.; Hamplová V.; Glogarová M.; Rychetský I.; Pociecha D. *Liq. Cryst.* **2004**, *31*, 1131–1141.
(14) Bubnov A.; Hamplová V.; Kašpar M.; Glogarová M.; Vaněk P. *Ferroelectrics* **2000**, *243*, 27–35.
(15) Hamplová V.; Bubnov A.; Kašpar M.; Novotná V.; Glogarová M. *Liq. Cryst.* **2003**, *30*, 493–497.
(16) Novotná V.; Kašpar M.; Hamplová V.; Glogarová M.; Bílková P.; Domenici V.; Pociecha D. *Liq. Cryst.* **2008**, *35*, 287–298.
(17) Goodby J.W.; Slaney A.J.; Booth C.J.; Nishiyama I.; Vuijk J.D.; Styring P.; Toyne K.J. *Mol. Cryst. Liq. Cryst.* **1994**, *243*, 231–298.
(18) Henderson P.A.; Drzewinski W.; Dabrowski R. *Ferroelectrics* **2006**, *343*, 11–18.
(19) Pyzuk W.; Górecka E.; Szydłowska J.; Krowczynski A.; Pociecha D. *Phys. Rev. E* **1995**, *52*, 1748–1752.
(20) Dierking I. *Textures of Liquid Crystals*; Wiley-VCH Verlag: Weinheim, 2003.
(21) Lagerwall J.P.F.; Giesselmann F. *Phys. Rev. E* **2002**, *66*, 031703.
(22) Takanishi Y.; Ikeda A.; Takezoe H.; Fukuda A. *Phys. Rev. E* **1995**, *51*, 400.
(23) Goodby J.W. *Struct. Bonding* **1999**, *95*, 84–147.
(24) Ikeda A.; Takanishi Y.; Takezoe H.; Fukuda A. *Jap. J. Appl. Phys.* **1993**, *32*, L97–L100.
(25) Čepič M.; Žekš B. *Mol. Cryst. Liq. Cryst.* **1995**, *A236*, 61–67.
(26) Škarabot M.; Čepič M.; Žekš B.; Blinc R.; Heppke G.; Kityk A.V.; Muševič I. *Phys. Rev. E* **1998**, *58*, 575–584.
(27) Ismaili M.; Bougrioua F.; Isaert N.; Legrand C.; Nguyen H.T. *Phys. Rev. E* **2001**, *65*, 011701 (1–8).
(28) Muševič I.; Blinc R.; Žekš B. *The Physics of Ferroelectric and Antiferroelectric Liquid Crystals*; World Scientific: 2000.
(29) Panarin Y.; Kalinovskaya O.; Vij J. *Liq. Cryst.* **1998**, *25*, 241.
(30) Buivydas M.; Gouda F.; Anderson G.; Lagerwall S.; Stebler B. *Liq. Cryst.* **1997**, *23*, 723–739.

(31) Hou J.; Schacht J.; Giesselmann F.; Zugenmaier P. *Liq. Cryst.* **1997**, *22*, 409–417.
(32) Glogarová M.; Pociecha D.; Gorecka E.; Rychetský I.; Mieczkowski J. *Ferroelectrics* **2000**, *245*, 43–50.
(33) Parry-Jones L.A.; Elston S.J. *Phys. Rev. E* **2001**, *63*, 050701R (1–4).
(34) Parry-Jones L.A.; Elston S.J. *J. Appl. Phys.* **2002**, *92*, 449–455.
(35) Bubnov A.; Hamplová V.; Kaspar M.; Vanek P.; Pociecha D.; Glogarová M. *Mol. Cryst. Liq. Cryst.* **2001**, *366*, 547–556.
(36) Kaspar M.; Hamplová V.; Pakhomov S.A.; Stibor I.; Sverenyák H.; Bubnov A.M.; Glogarová M.; Vanek P. *Liq. Cryst.* **1997**, *22*, 557–561.
(37) Dabrowski R.; Drzewinski W.; Dziaduszek J.; Gasowska J.; Henderson P.A.; Kula P.; Oton J.M.; Bennis N. *Opto-electron. Rev.* **2007**, *15*, 32–36.